RESEARCH ARTICLE

Check for updates

Dopant-mediated carrier tunneling in short-channel two-dimensional transistors†

Yue Lu, [iD] ‡[a] Chenyu Li,‡[a] Shenbo Yang,[b] Mingxuan Yuan,[a] Shuo Qiao[a] and Qingqing Ji [iD] *[a]

Substitutional doping has played a pivotal role in silicon-based electronics and holds equivalent importance for emerging two-dimensional (2D) semiconductors, which show promise for advanced node technologies. However, the intricate role of dopant atoms in 2D transistors, particularly in short-channel cases, remains elusive and poses a challenging task for experimental exploration. In this study, using density functional theory (DFT) calculations and quantum transport simulations, we reveal the dual functionalities of V dopants in short-channel 2D transistors constructed with lateral $VS_2–MoS_2–VS_2$ heterostructures. Depending on the channel length, the V dopant in the MoS_2 channel, manifested by localized density of states (LDOS), can serve as either a "relay station" to facilitate carrier tunneling or as a scattering center that reduces source-drain currents. This work hence provides valuable insights into the doping effect of short-channel 2D transistors, and opens up possibilities for new electronic applications that harness the delicate properties of these substitutional dopants.

Introduction

As the channel lengths (L_{ch}) of silicon-based transistors decrease, the short-channel effects become increasingly severe, limiting their application potential for advanced-node integrated circuitry.[1,2] Exploring new materials and technologies to overcome these challenges has become an urgent demand.[3,4] 2D semiconductors, such as monolayer molybdenum disulfide (MoS_2), possess remarkable electrical properties even at atomic thickness, making them highly promising for short-channel electronic devices.[5–7] This potential has been exemplified by using ultrascaled gate electrodes such as 1-nm-wide carbon nanotubes[8] and 0.34-nm-wide graphene edges,[9] both of which demonstrate effective field-effect transistor (FET) switching.

Nevertheless, MoS_2 as a native n-type semiconductor is by itself insufficient for constructing low-power complementary metal–oxide–semiconductor (CMOS) circuits. To realize the desired CMOS logic functions and computations, it is crucial to achieve p-type carrier conduction in MoS_2, for which strategies have been proposed through contact engineering[10–12] or substitutional doping.[13–15] Elements such as V, Nb, and Ta with one less valence electron than Mo are the commonly used

p-type dopants.[16–20] However, due to the weak dielectric screening of the monolayer system,[21] releasing charge carriers from the ionizable dopants is inefficient, for which variable-range hopping (VRH) has been proposed as the dominant mechanism for electrical conductance.[13] In ultrascaled MoS_2 transistors, the effectiveness of this VRH mechanism vanishes, necessitating the resolution of short-channel transport properties, particularly in the presence of atomic dopants.

Conventionally, doped atoms are typically considered analogous to point defects, which, at the macroscopic level, can regulate carrier concentration, act as carrier scattering centers,[22] and serve as charge traps that affect carrier lifetimes.[23] However, when device dimensions are reduced to the nanoscale, these point defects can possibly exhibit new electronic functionalities. For instance, the changes in local potential barriers introduced by these defects can significantly influence the quantum transport of carriers, exemplified as single-atom transistors.[24] To this point, the impact of heteroatoms on the transport properties of doped MoS_2 has been explored at microdevice levels, but their role in the short-channel regime remains unknown.

The aforementioned task is quite challenging in experiments because of the limited spatial resolution of current nanofabrication techniques. Otherwise, endeavors in synthesizing lateral heterostructures have resulted in 2D transistors with sub-micron L_{ch}.[25] To this end, first-principles calculations based on density functional theory (DFT), in combination with the non-equilibrium Green's function (NEGF) method, have offered theoretical predictions on the transport characteristics of short-channel MoS_2 transistors,[26–29] indicating, for instance,

[a] *School of Physical Science and Technology, ShanghaiTech University, Shanghai 201210, China. E-mail: jiqq@shanghaitech.edu.cn*

[b] *Hongzhiwei Technology (Shanghai) Co., Ltd., Shanghai 201210, China*

‡ These authors contribute equally to this work.

a lower L_{ch} limit of 2.7 nm to inhibit source-drain tunneling.[30] The incorporation of V dopants in the simulated MoS_2 channels should be highly feasible, and could contribute to establishing the relationship between substitutional doping and transport properties, which, to our knowledge, remains to be explored.

In this theoretical study, we explore the impact of V dopants on the transport characteristics of short-channel MoS_2 transistors, utilizing VS_2 as the source/drain electrodes and V-doped MoS_2 (V-MoS_2) as the channel material. Our calculations demonstrate that, the incorporation of V dopants modifies the valence band edge by introducing a localized state, which, according to our transport simulations, manifests dual functionalities of either promoting or scattering the carrier flow, depending on the L_{ch}. This work hence highlights the crucial role of substitutional doping in shaping the transport properties of short-channel 2D transistors, and offers potential avenues for novel electronic applications that leverage the delicate properties of these atomic dopants.

Calculation methods

The crystal and device models were constructed with Device Studio (DS),[31] and electronic property calculations were performed on the basis of DFT,[32] using the DS-PAW[33] and Nanodcal[34] software integrated within the DS platform. The Perdew–Burke–Ernzerhof (PBE) functional under the generalized gradient approximation (GGA) was employed to describe the exchange correlation interaction.[35,36] The plane wave basis set was truncated at a cutoff energy of 450 eV. To avoid interlayer interactions, a vacuum spacing of 20 Å was employed in the z-direction of both the crystal and device models. A k-point mesh of $7 \times 7 \times 1$ was used to sample the Brillouin zone for band structure calculations. To achieve an optimal interface structure, we fixed the positions of other atoms and fully relaxed the four rows of atoms on both sides of the interface, using a k-point mesh of $1 \times 3 \times 1$ and a force convergence criterion of 0.02 eV Å^{-1}.

Transport properties of the simulated devices were calculated by Nanodcal that encodes the NEGF method.[37] The valence electron orbitals were described using the double-zeta plus polarization (DZP) basis set, with a cutoff energy of 80 Hartree. The Monkhorst–Pack method was used for Brillouin zone sampling,[38] with a $1 \times 6 \times 1$ k-point mesh for the central region and a $10 \times 6 \times 1$ k-point mesh for the electrode regions. The energy convergence criteria were set to 10^{-4} eV. A $1 \times 100 \times 1$ k-point mesh was used to calculate currents and electron transmission spectra at 300 K, using the Landauer-Büttiker formula:[39]

$$I(V) = \frac{2e}{hT} \int_{\mu_L}^{\mu_R} T(E, V_b)[f_L(E, \mu_L) - f_R(E, \mu_R)]dE \quad (1)$$

where V_b is the bias voltage, $T(E,V_b)$ is the transmission coefficient, $f(E,\mu)$ and μ are the Fermi–Dirac distribution function and chemical potential, respectively, with the subscript L(R) representing the drain (source) electrode. Following previous literature,[40] we have also examined the transport properties with and without resolving the

spin states for the calculated systems, and provided them in Fig. S1 and related discussion in the ESI.†

Results and discussion

The optimized structure of MoS_2, as shown in Fig. 1a and inset of Fig. 1c, demonstrates a Mo–S bond length of 2.414 Å and a S–Mo–S bond angle of 80.702°, together with a minimum Mo–Mo distance of 3.19 Å consistent with reported results.[41] In the case of V-MoS_2, where V is trigonal-prismatically coordinated (Fig. 1d), the less electronegativity of V compared to Mo contributes to greater polarization of the V–S bonds, resulting in reduced bond length of 2.365 Å and increased S–V–S bond angle of 80.893°, also in agreement with previous reports.[42]

To verify the p-type doping effect of V dopants, we calculated the projected band structures and projected densities of states (PDOS) for both pristine MoS_2 and V-MoS_2. The pristine MoS_2 exhibits fully occupied valence band and an intrinsic bandgap of 1.65 eV, whose band edges mainly originate from the non-bonding d orbitals of Mo atoms (Fig. 1b and c). In contrast, the V-MoS_2 shows prominent features of a p-type semiconductor, with the Fermi level (E_F) slightly intersects the valence band (Fig. 1e and f). Notably, our orbital projection analysis further reveals that the topmost valence band mainly originates from the V atom and contributes to a pronounced peak at E_F in the PDOS spectra, as marked by the dash orange box in Fig. 1e and f. It is foreseeable that in V-MoS_2 short-channel transistors, the presence of this conspicuous doping peak will exert a noteworthy influence on the charge transport properties, which is the focus of the present work.

In addition, 1T-VS_2, an air-stable metallic 2D material,[43] has also been modeled and theoretically calculated. As shown in Fig. 1g and inset of Fig. 1i, the optimized structure of VS_2 exhibits lattice parameters consistent with literature reports[44] and close to that of MoS_2. Band structure and PDOS analyses of VS_2 (Fig. 1h and i) reveal no bandgap and a high density of states at E_F, confirming its metallic property. For now, we are ready to investigate the short-channel transport properties of pristine MoS_2 and V-MoS_2, using VS_2 as the electrode material.

The configuration of the FET device is illustrated in Fig. 2a. Two semi-infinitely long 1T-VS_2 electrodes were utilized, ensuring that the electrode region maintains a macroscopic potential under the shielding approximation. The central region is composed of V-MoS_2, which exhibits a finite size along the transport direction, satisfying the short-channel condition. One-dimensional in-plane periodic boundary conditions were imposed perpendicular to the transport direction to eliminate edge effects. Sufficient buffer layers were introduced between the channel and the electrodes to ascertain the wavefunction continuity at the channel/electrode interface, which was further confirmed by the potential profile analysis (Fig. S2, ESI†). Additionally, two virtual gate electrodes with an equivalent oxide thickness of 0.5 nm were placed above and below the central region to modulate the E_F of the channel material.

As depicted in Fig. 2b and c, we firstly calculated the real-space DOS (@ −0.2 eV) of the V-MoS_2 transistor (L_{ch} = 3.0 nm)
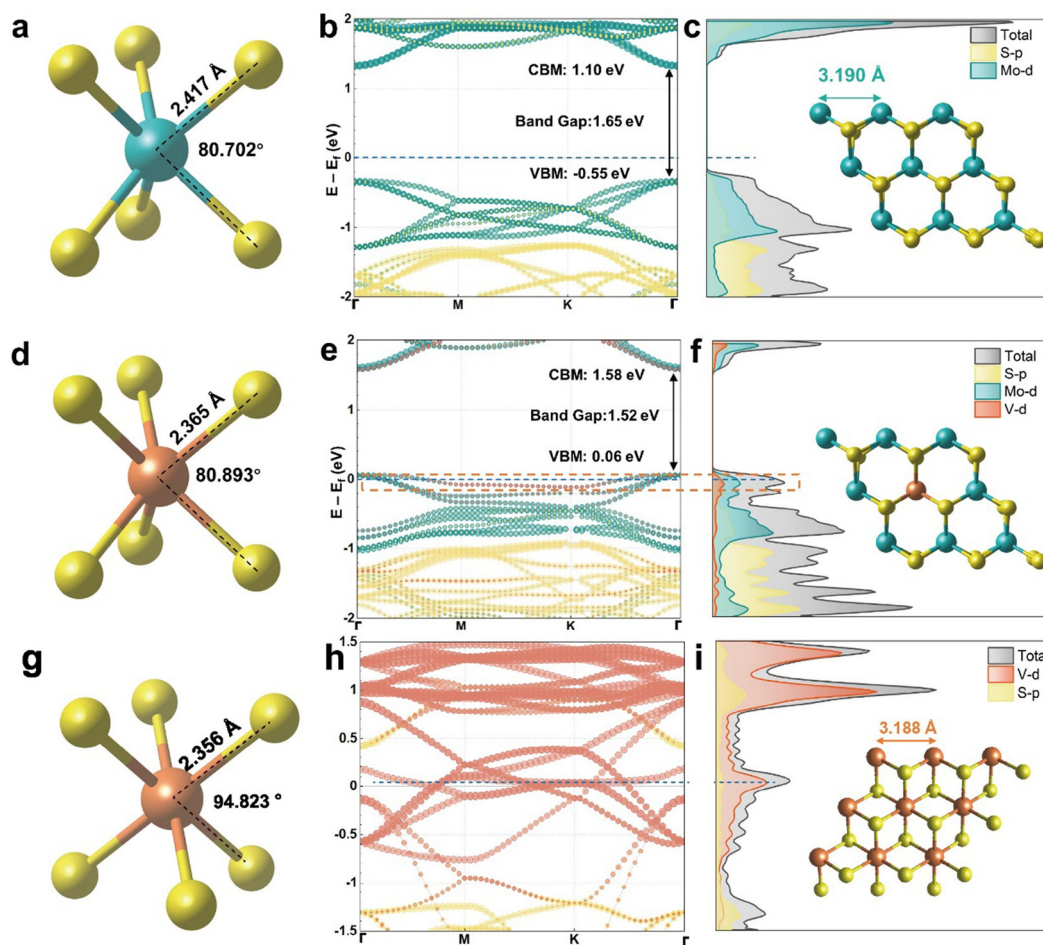
Fig. 1 Crystal structure and electronic properties. Atomic structures of MoS_2 (a), V-MoS_2 (d), and VS_2 (g) are schematically illustrated, showing the S–M bond length and the S–M–S bond angle, where M represents Mo or V. The Mo, V, and S atoms are shown in blue, orange, and yellow, respectively. Band structures and PDOS of MoS_2 (b) and (c), V-MoS_2 (e) and (f), and VS_2 (h) and (i) are also presented. The insets in the PDOS spectra correspond to the respective crystal cell models.

to gain insights into its electronic characteristics. The localized nature of the V-doping state with a spanning size of ∼0.8 nm can be clearly visualized, showing finite influence only on the six nearest-neighboring Mo atoms. Corresponding PDOS profile of the device also verified the localization of the doping state, which is absent in pristine MoS_2 (Fig. S3, ESI†). By plotting the differential charge density around the V dopant (inset of Fig. 2b), it is evident that the V atom undergoes electron exchange with three nearest S atoms and six second-nearest Mo atoms, whilst the third-nearest S atoms are barely affected. Besides, the differential charge density of the Mo atoms exhibits a similar pattern to the LDOS distribution (highlighted by the red box in Fig. 2b and c), possibly suggesting that direct d orbital hybridization is responsible for the finite spanning of the V-doping state.

The contact characteristics are of critical importance for device transport.[45] As shown in Fig. S4 (ESI†), the interface between VS_2 and MoS_2 manifests a p-type Schottky contact, exhibiting a Schottky barrier height of 0.63 eV, whereas the heterojunction formed between V-MoS_2 and VS_2 displays a quasi–Ohmic contact. Detailed discussion on the contact

properties is provided in ESI.† To comprehensively investigate the doping effect on short-channel charge transport, a series of V-MoS_2 transistors were constructed and simulated, with varied L_{ch} ranging from 1.2 nm to 4.2 nm (Fig. 3a–f). A bias voltage of 0.2 V was applied to the source electrodes to drive the current flow across the channels. For comparison, devices with pristine MoS_2 channels were also simulated. The transfer curves for all the devices clearly demonstrate the p-type doping effect of V atoms on MoS_2, as evidenced by higher hole conductance at $V_g = 0$ V compared to pristine MoS_2. At smallest L_{ch} of 1.2 nm and 1.8 nm, the smooth transfer curves (Fig. 3a and b), combined with the higher on-state currents of V-MoS_2 compared to pristine MoS_2, suggest an efficient source–drain tunneling and the absence of charge scattering at the V-doped site. Notably, at intermediate L_{ch} of 2.4 nm and 3.0 nm, discernible current bulges appear in the subthreshold regions (indicated by the dash lines in Fig. 3c and d), likely associated with the existence of localized V-doping states. Similar dome-shaped transport characteristics have been experimentally observed in V-doped WSe_2 monolayers,[46] where the presence of V impurity states near the valence-band edge was also inferred as the key factor. Our transport simulation hence
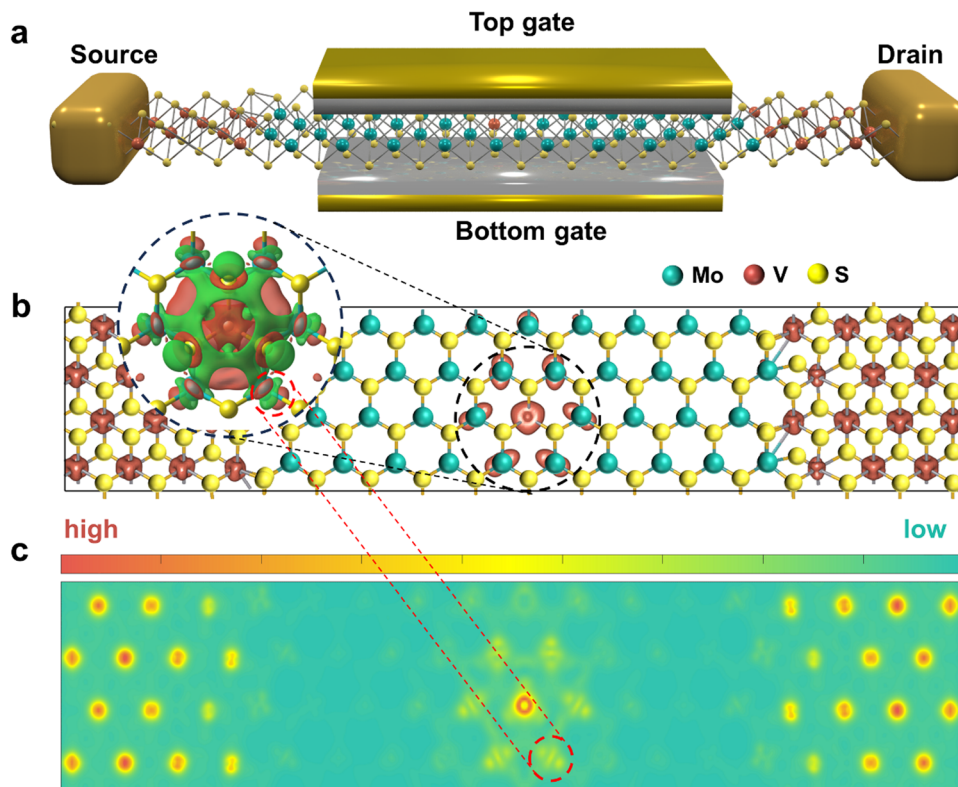
Fig. 2 Schematic diagram of a FET model with VS_2 electrodes at both ends, V-MoS_2 channel in the middle (L_{ch} =3.0 nm), and gate electrodes (EOT = 0.5 nm) on top and bottom (a). The real-space DOS at −0.2 eV (b) and corresponding 2D plot (c) are shown with zero source-drain bias applied. The inset in (b) represents the differential charge density at the V-doped site.

captures the essential characteristics of doped 2D systems, hinting on new device physics at ultimate length scales.

However, with the L_{ch} further increased, the bulging feature for V-MoS_2 was concealed by current fluctuations (Fig. 3e and f), along with the reduced on-state currents (Fig. 3g). While the off-state currents for both V-MoS_2 and MoS_2 transistors show similar monotonic evolution depending on L_{ch} (Fig. 3h), the decrease of on-state currents for V-MoS_2 leads to a saturation behavior in the on/off ratios (Fig. 3i), highly suggesting that charge scattering predominantly affects the transport properties of V-MoS_2 at these channel lengths. A detailed physical picture was elucidated in the context of random telegraph noise[47,48] for short-channel MoS_2 transistors, which incorporated the dynamics of charge capture and emission by unspecified atomic defects. Besides, subthreshold swings and field-effect mobilities of both the V-MoS_2 and MoS_2 transistors at different channel lengths were extracted from the simulated transfer curves in Fig. 3a–f, which further highlight the electronic role of V dopants (Fig. S5, ESI†). Overall, our first-principles calculations reveal an L_{ch}-dependent electronic effect associated with the V dopants, contributing to anomalous current peaks at intermediate L_{ch}, while causing scattering of charge carriers at $L_{ch} \geq 3.6$ nm.

Since charge scattering by atomic impurities is a well-recognized phenomenon, we mainly focus on illustrating the origin of the anomalous current peak in the subthreshold region. For this purpose, the V-MoS_2 transistor with

L_{ch} = 3.0 nm was further elucidated by the PDOS profiles (Fig. S6, ESI†) and corresponding transmission spectra (Fig. S7, ESI†), under a constant source-drain bias (V_{sd} = 0.2 V) and varied gate voltages (V_g). We note that only those transmission coefficients within the bias window of −0.2 eV to 0 eV contribute to the source-drain current.

At V_g = 0.7 V, the bias window intersects the bandgap, providing no states in the channel to accommodate charge carriers. Due to the sufficient L_{ch}, direct source-drain tunneling was inhibited, leading to small integrated transmission probability and an "off-state" of the device, as depicted in Fig. 4a. As V_g gradually decreased, the energy bands of the channel material underwent continuous elevation, causing the bias window to overlap with the V-doping state at V_g = 0 V (Fig. 4b). The relatively short distance between the dopant and the electrodes (half of the L_{ch}) facilitated effective tunneling, allowing the dopant site to act as a "relay station" for charge carriers. This contributes to a "high-transmission state" from the source to the drain, manifesting a conductance peak in the subthreshold region (Fig. 3d), a phenomenon we refer to as "assisted tunneling".

However, as V_g further decreased to −0.2 V, the integrated transmission probability diminished from 1.14×10^{-6} (at V_g = 0 V) to 1.72×10^{-7} (Fig. 4c). This behavior arises from the dual functionality of the V-doping site, which not only facilitates assisted tunneling but also induces charge scattering, as illustrated by the real-space DOS image in Fig. 4c. Specifically, at V_g = −0.2 V, holes around the V atom accumulated by the gating
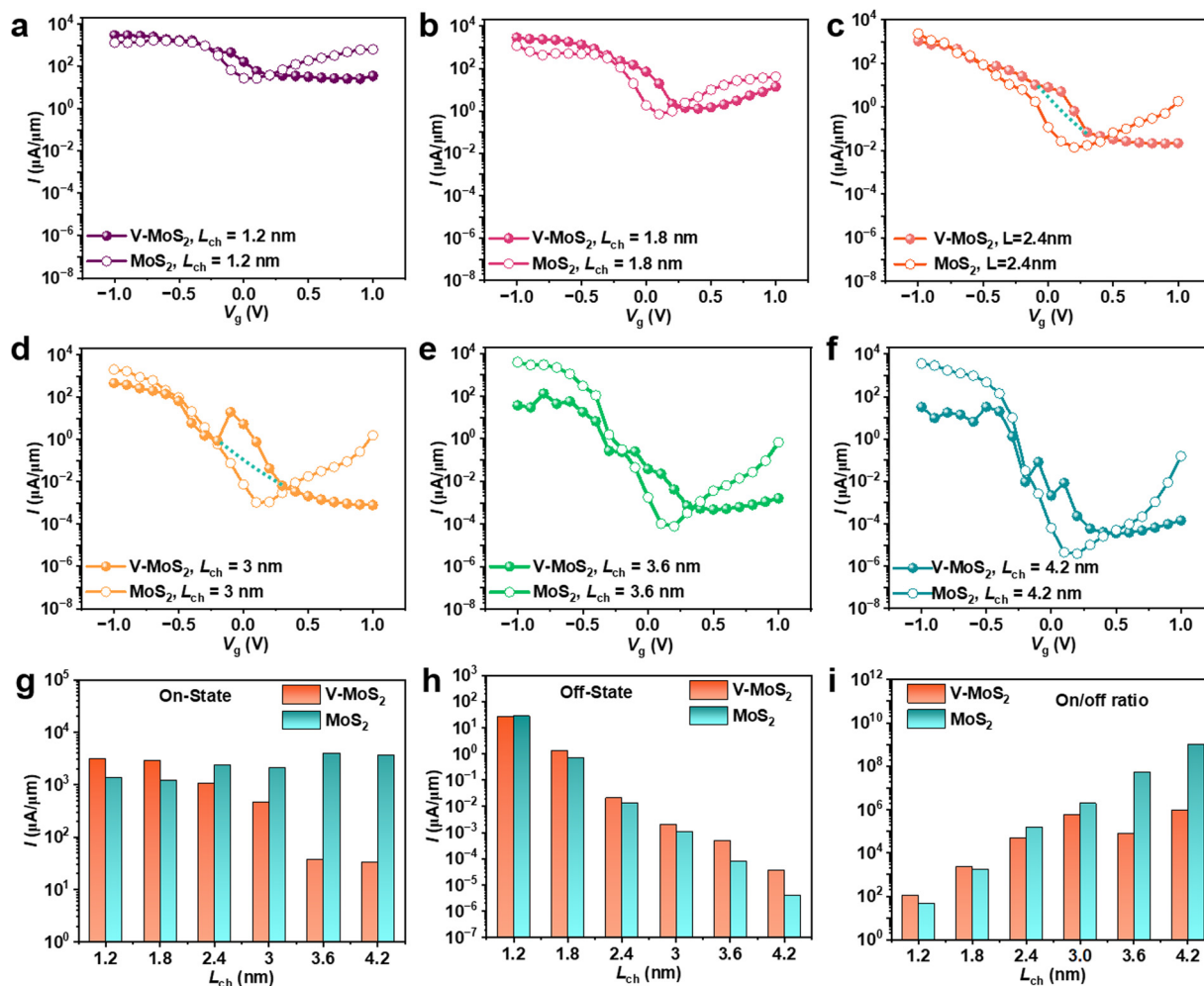
Fig. 3 (a)–(f) Transfer characteristics of MoS_2 (hollow circles) and V-MoS_2 (solid spheres) at L_{ch} = 1.2 nm (a), 1.8 nm (b), 2.4 nm (c), 3.0 nm (d), 3.6 nm (e), and 4.2 nm (f), under a source bias of 0.2 V. Shown in (g-i) are the comparison of the on-state currents (g), off-state currents (h), and on/off ratios (i) between V-MoS_2 (orange) and MoS_2 (cyan) at different L_{ch}.

effect depleted the localized doping state and repelled positive charges, thereby preventing to some extent carrier tunneling from the source to the dopant. Even though drift transport occurred from the dopant to the drain, the overall channel conductance decreased, resulting in a "low-transmission state" and the inflection point observed in the transfer curve (Fig. 3d). With V_g decreased to −0.6 V, the valence band of the MoS_2 channel started to enter the bias window, enabling carriers to drift through the entire channel and transitioning the device into the "on-state" (Fig. 4d). In this case, the V-doping site with enriched and trapped holes acted as a charge scattering center, reducing the on-state currents compared to pristine MoS_2.

Schematic band diagrams are plotted in Fig. 5 to further elucidate the electronic functionalities of V-doped states at different channel lengths. As depicted in Fig. 5a and b, when the channel length is less than 1.8 nm, the carriers can tunnel directly between the two electrodes, and the V-doped states play a supporting role on enhancing the tunneling probability. When the channel length is in the range of 2.4–3.0 nm (Fig. 5c and d), direct carrier tunneling between the electrodes

is suppressed; in this case, the V-doped sites act as "repeaters" that facilitate assisted tunneling, leading to an anomalous transconductance peak in the subthreshold region. Importantly, even considering spin polarization of the dopant states, the assisted-tunneling effect was still valid, manifesting two kinks in the subthreshold region that can be ascribed to the Coulomb splitting effect of the spin-polarized state.[49] When the channel length exceeds 3.6 nm (Fig. 5e and f), the V-doped sites can no longer afford assisted tunneling, and instead, they act as impurity scattering centers that imped the carrier transport.

Conclusion

In summary, we have uncovered the electronic effects of heteroatom dopants in short-channel 2D transistors, using a combination of first-principles calculations and quantum transport simulations. By employing lateral VS$_2$–MoS_2–VS$_2$ heterostructures as the model system, we show that the implanted V dopants in the MoS_2 channels manifest dual electronic
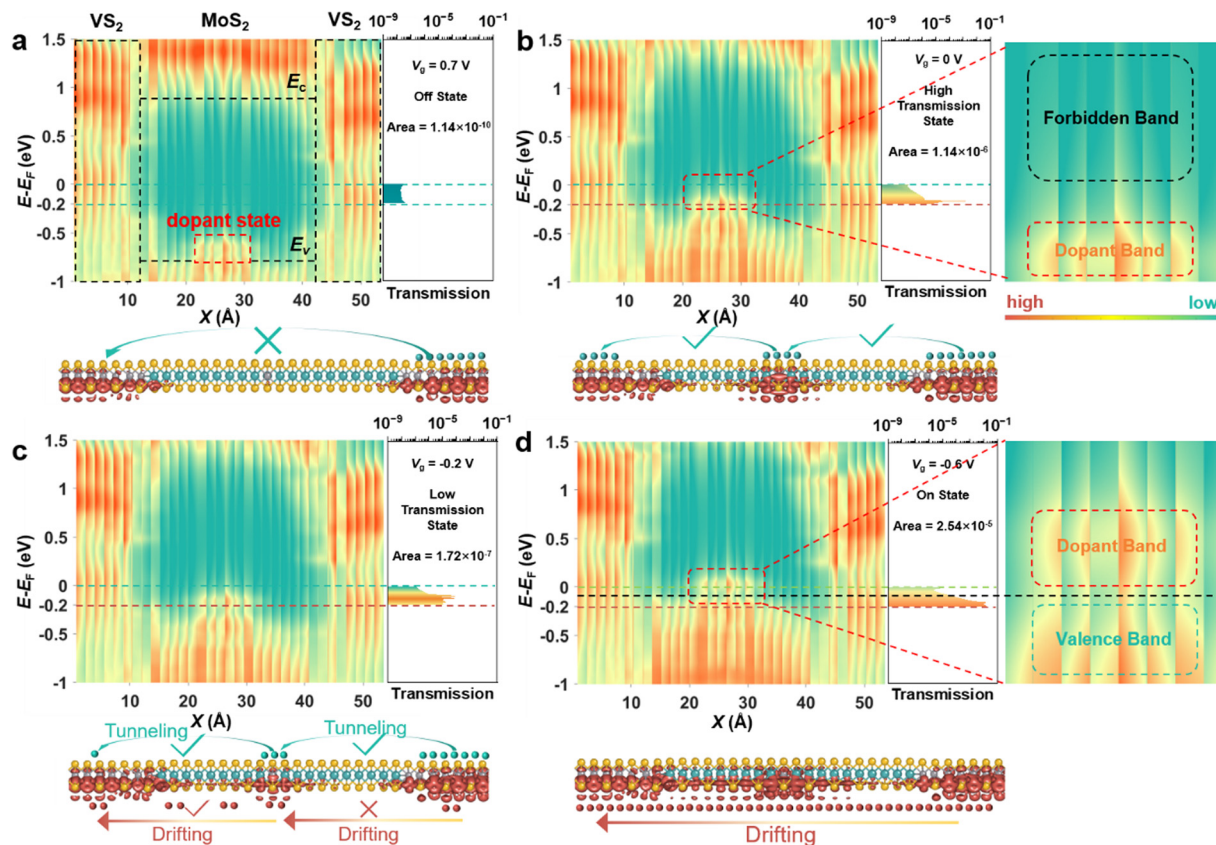
Fig. 4 PDOS profiles, electron transmission spectra, and real-space DOS at -0.2 eV of a V-MoS$_2$ transistor, with L_{ch} = 3.0 nm and V_{sd} = 0.2 V, calculated under different gate voltages (V_g) of 0.7 V (a), 0 V (b), −0.2 V (c), and −0.6 V. Insets on the right of (b) and (d) show magnified views of the forbidden band, the dopant band, and the valence band in the PDOS profiles. The orange arrows (balls) indicate drift transport (holes), while the cyan arrows (balls) denote tunneling transport (holes).
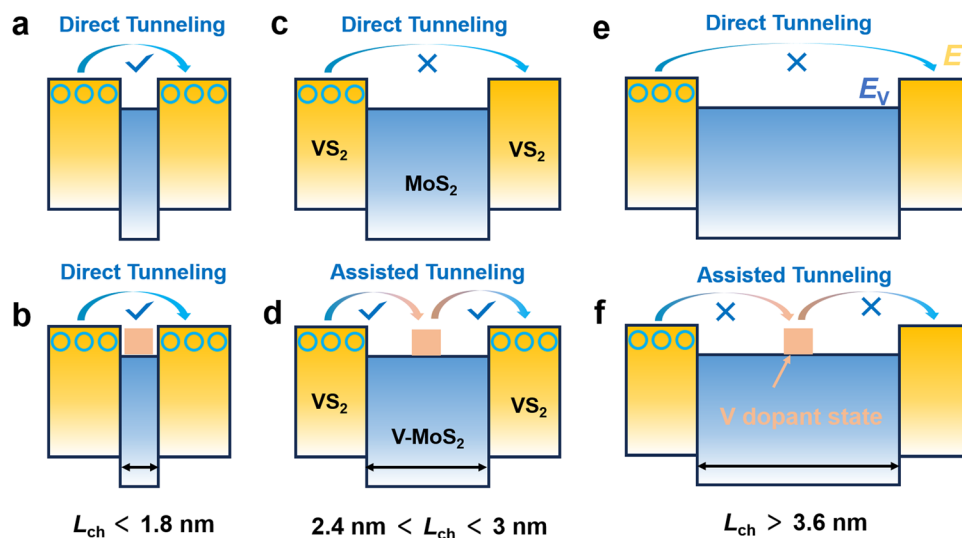

Fig. 5 Schematic illustration on the electronic functionalities of the V-doped states at different channel lengths. Band diagrams of MoS$_2$ and V-MoS$_2$ at L_{ch} < 1.8 nm (a, b), 2.4 nm < L_{ch} < 3.0 nm (c, d) and L_{ch} > 3.6 nm (e) and (f) are plotted. The blue hollow circles represent holes. The yellow and blue regions signify the VS$_2$ electrodes and the MoS$_2$ channel, respectively. The orange regions represent the V-doped states at the top of the MoS$_2$ valence band.

functionalities, either promoting source–drain currents through assisted tunneling, or acting as scattering centers to reduce the channel conductance. The trade-off of the two competing

electronic effects can be modulated by varying the channel lengths in the sub-10 nm range. Such L_{ch}-dependent electronic functionalities differ from the known mechanisms of carrier
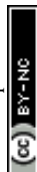
doping and impurity scattering[22] caused by point defects, offering possibility of designed electronics at these extreme length scales, such as atomic Boltzmann machines[50] and dopant-atom networks.[51]

Data availability

The authors confirm that the data supporting the findings of this study are available within the article and its ESI.†

Conflicts of interest

There are no conflicts to declare.

Acknowledgements

References

1 R. Chau, B. Doyle, S. Datta, J. Kavalieros and K. Zhang, Integrated nanoelectronics for the future, *Nat. Mater.*, 2007, **6**, 810–812.

2 T. N. Theis and P. M. Solomon, It's Time to Reinvent the Transistor, *Science*, 2010, **327**, 1600–1601.

3 A. D. Franklin, Nanomaterials in transistors: From high-performance to thin-film applications, *Science*, 2015, **349**, aab2750.

4 D. Akinwande, C. Huyghebaert, C.-H. Wang, M. I. Serna, S. Goossens, L.-J. Li, H. S. P. Wong and F. H. L. Koppens, Graphene and two-dimensional materials for silicon technology, *Nature*, 2019, **573**, 507–518.

5 B. Radisavljevic, A. Radenovic, J. Brivio, V. Giacometti and A. Kis, Single-layer MoS_2 transistors, *Nat. Nanotechnol.*, 2011, **6**, 147–150.

6 M. Chhowalla, D. Jena and H. Zhang, Two-dimensional semiconductors for transistors, *Nat. Rev. Mater.*, 2016, **1**, 16052.

7 Y. Liu, X. Duan, H.-J. Shin, S. Park, Y. Huang and X. Duan, Promises and prospects of two-dimensional transistors, *Nature*, 2021, **591**, 43–53.

8 S. B. Desai, S. R. Madhvapathy, A. B. Sachid, J. P. Llinas, Q. Wang, G. H. Ahn, G. Pitner, M. J. Kim, J. Bokor, C. Hu, H. S. P. Wong and A. Javey, MoS_2 transistors with 1-nanometer gate lengths, *Science*, 2016, **354**, 99–102.

9 F. Wu, H. Tian, Y. Shen, Z. Hou, J. Ren, G. Gou, Y. Sun, Y. Yang and T.-L. Ren, Vertical MoS_2 transistors with sub-1-nm gate lengths, *Nature*, 2022, **603**, 259–264.

10 S. Chuang, C. Battaglia, A. Azcatl, S. McDonnell, J. S. Kang, X. Yin, M. Tosun, R. Kapadia, H. Fang, R. M. Wallace and A. Javey, MoS_2 P-type Transistors and Diodes Enabled by High Work Function MoO_x Contacts, *Nano Lett.*, 2014, **14**, 1337–1342.

11 C. Dorow, K. O'Brien, C. H. Naylor, S. Lee, A. Penumatcha, A. Hsiao, T. Tronic, M. Christenson, K. Maxey, H. Zhu, A. Oni, U. Alaan, T. Gosavi, A. S. Gupta, R. Bristol, S. Clendenning, M. Metz and U. Avci, Advancing Monolayer 2-D nMOS and pMOS Transistor Integration From Growth to van der Waals Interface Engineering for Ultimate CMOS Scaling, *IEEE Trans. Electron Devices*, 2021, **68**, 6592–6598.

12 Y. Wang, J. C. Kim, Y. Li, K. Y. Ma, S. Hong, M. Kim, H. S. Shin, H. Y. Jeong and M. Chhowalla, P-type electrical contacts for 2D transition-metal dichalcogenides, *Nature*, 2022, **610**, 61–66.

13 H. Gao, J. Suh, M. C. Cao, A. Y. Joe, F. Mujid, K.-H. Lee, S. Xie, P. Poddar, J.-U. Lee, K. Kang, P. Kim, D. A. Muller and J. Park, Tuning Electrical Conductance of MoS_2 Monolayers through Substitutional Doping, *Nano Lett.*, 2020, **20**, 4095–4101.

14 Y.-C. Lin, R. Torsi, D. B. Geohegan, J. A. Robinson and K. Xiao, Controllable Thin-Film Approaches for Doping and Alloying Transition Metal Dichalcogenides Monolayers, *Adv. Sci.*, 2021, **8**, 2004249.

15 A. Kozhakhmetov, S. Stolz, A. M. Z. Tan, R. Pendurthi, S. Bachu, F. Turker, N. Alem, J. Kachian, S. Das, R. G. Hennig, O. Gröning, B. Schuler and J. A. Robinson, Controllable p-Type Doping of 2D WSe_2 via Vanadium Substitution, *Adv. Funct. Mater.*, 2021, **31**, 2105252.

16 J. Suh, T. L. Tan, W. Zhao, J. Park, D.-Y. Lin, T.-E. Park, J. Kim, C. Jin, N. Saigal, S. Ghosh, Z. M. Wong, Y. Chen, F. Wang, W. Walukiewicz, G. Eda and J. Wu, Reconfiguring crystal and electronic structures of MoS_2 by substitutional doping, *Nat. Commun.*, 2018, **9**, 199.

17 L. Zhang, G. Wang, Y. Zhang, Z. Cao, Y. Wang, T. Cao, C. Wang, B. Cheng, W. Zhang, X. Wan, J. Lin, S.-J. Liang and F. Miao, Tuning Electrical Conductance in Bilayer MoS_2 through Defect-Mediated Interlayer Chemical Bonding, *ACS Nano*, 2020, **14**, 10265–10275.

18 J. Zhang, Y. Zhu, M. Tebyetekerwa, D. Li, D. Liu, W. Lei, L. Wang, Y. Zhang and Y. Lu, Vanadium-Doped Monolayer MoS_2 with Tunable Optical Properties for Field-Effect Transistors, *ACS Appl. Nano Mater.*, 2021, **4**, 769–777.

19 M. Li, X. Wu, W. Guo, Y. Liu, C. Xiao, T. Ou, Y. Zheng and Y. Wang, Controllable p-type doping of monolayer MoS_2 with tantalum by one-step chemical vapor deposition, *J. Mater. Chem. C*, 2022, **10**, 7662–7673.

20 Z. Wang, M. Tripathi, Z. Golsanamlou, P. Kumari, G. Lovarelli, F. Mazziotti, D. Logoteta, G. Fiori, L. Sementa, G. M. Marega, H. G. Ji, Y. Zhao, A. Radenovic, G. Iannaccone, A. Fortunelli and A. Kis, Substitutional p-Type Doping in NbS_2–MoS_2 Lateral Heterostructures Grown by MOCVD, *Adv. Mater.*, 2023, **35**, 2209371.

21 J.-Y. Noh, H. Kim, M. Park and Y.-S. Kim, Deep-to-shallow level transition of Re and Nb dopants in monolayer MoS_2 with dielectric environments, *Phys. Rev. B: Condens. Matter Mater. Phys.*, 2015, **92**, 115431.

22 S. T. Pantelides, The electronic structure of impurities and other point defects in semiconductors, *Rev. Mod. Phys.*, 1978, **50**, 797–858.

23 E. Kamieniecki, Effect of charge trapping on effective carrier lifetime in compound semiconductors: High resistivity CdZnTe, *J. Appl. Phys.*, 2014, **116**, 193702.

24 M. Fuechsle, J. A. Miwa, S. Mahapatra, H. Ryu, S. Lee, O. Warschkow, L. C. L. Hollenberg, G. Klimeck and M. Y. Simmons, A single-atom transistor, *Nat. Nanotechnol.*, 2012, **7**, 242–246.

25 W. S. Leong, Q. Ji, N. Mao, Y. Han, H. Wang, A. J. Goodman, A. Vignon, C. Su, Y. Guo, P.-C. Shen, Z. Gao, D. A. Muller, W. A. Tisdale and J. Kong, Synthetic Lateral Metal-Semiconductor Heterostructures of Transition Metal Disulfides, *J. Am. Chem. Soc.*, 2018, **140**, 12354–12358.

26 Y. Yoon, K. Ganapathi and S. Salahuddin, How Good Can Monolayer MoS₂ Transistors Be, *Nano Lett.*, 2011, **11**, 3768–3773.

27 D. Marian, E. Dib, T. Cusati, E. G. Marin, A. Fortunelli, G. Iannaccone and G. Fiori, Transistor Concepts Based on Lateral Heterostructures of Metallic and Semiconducting Phases of MoS₂, *Phys. Rev. Appl.*, 2017, **8**, 054047.

28 Y. Zhao, Y. Li and F. Ma, Performance Upper Limit of Sub-10 nm Monolayer MoS₂ Transistors with MoS₂–Mo Electrodes, *J. Phys. Chem. C*, 2022, **126**, 12100–12112.

29 Z.-Q. Fan, X.-W. Jiang, J.-W. Luo, L.-Y. Jiao, R. Huang, S.-S. Li and L.-W. Wang, In-plane Schottky-barrier field-effect transistors based on 1T/2H heterojunctions of transition-metal dichalcogenides, *Phys. Rev. B*, 2017, **96**, 165402.

30 H. Lü, Y. Zhang, X. Liu, Y. Wang, Q. Zhang and H. Yin, Theoretical limit of how small we can make MoS₂ transistor channels, *J. Phys. D*, 2022, **55**, 105304.

31 Hongzhiwei Technology, Device Studio, Version 2023A, China, 2023, **https://cloud.hzwtech.com**.

32 G. Kresse and D. Joubert, From ultrasoft pseudopotentials to the projector augmented-wave method, *Phys. Rev. B: Condens. Matter Mater. Phys.*, 1999, **59**, 1758–1775.

33 P. E. Blöchl, Projector augmented-wave method, *Phys. Rev. B: Condens. Matter Mater. Phys.*, 1994, **50**, 17953–17979.

34 J. Taylor, H. Guo and J. Wang, Ab initio modeling of quantum transport properties of molecular electronic devices, *Phys. Rev. B: Condens. Matter Mater. Phys.*, 2001, **63**, 245407.

35 J. P. Perdew and W. Yue, Accurate and simple density functional for the electronic exchange energy: Generalized gradient approximation, *Phys. Rev. B*, 1986, **33**, 8800–8802.

36 J. P. Perdew, J. A. Chevary, S. H. Vosko, K. A. Jackson, M. R. Pederson, D. J. Singh and C. Fiolhais, Atoms, molecules, solids, and surfaces: Applications of the generalized gradient approximation for exchange and correlation, *Phys. Rev. B: Condens. Matter Mater. Phys.*, 1992, **46**, 6671–6687.

37 M. Brandbyge, J.-L. Mozos, P. Ordejón, J. Taylor and K. Stokbro, Density-functional method for nonequilibrium electron transport, *Phys. Rev. B: Condens. Matter Mater. Phys.*, 2002, **65**, 165401.

38 H. J. Monkhorst and J. D. Pack, Special points for Brillouin-zone integrations, *Phys. Rev. B: Solid State*, 1976, **13**, 5188–5192.

39 M. Büttiker, Y. Imry, R. Landauer and S. Pinhas, Generalized many-channel conductance formula with application to small rings, *Phys. Rev. B: Condens. Matter Mater. Phys.*, 1985, **31**, 6207–6215.

40 Y. Zhang, X. Chen, Y. Huang, C. Zhang, F. Li and H. Shu, The Role of Intrinsic Defects in Electrocatalytic Activity of Monolayer VS₂ Basal Planes for the Hydrogen Evolution Reaction, *J. Phys. Chem. C*, 2017, **121**, 1530–1536.

41 D. Yang, J. Jiang, J. Chen, X. Guo, X. Yang, X. Zheng, C. Deng, H. Xie, F. Song, F. Ouyang, X. Yuan, M. Chen and H. Huang, In-plane anisotropy in van der Waals epitaxial MoS₂ on MoO₂(010), *Appl. Phys. Lett.*, 2023, **122**, 111602.

42 I. Williamson, S. Li, A. Correa Hernandez, M. Lawson, Y. Chen and L. Li, Structural, electrical, phonon, and optical properties of Ti- and V-doped two-dimensional MoS₂, *Chem. Phys. Lett.*, 2017, **674**, 157–163.

43 Q. Ji, C. Li, J. Wang, J. Niu, Y. Gong, Z. Zhang, Q. Fang, Y. Zhang, J. Shi, L. Liao, X. Wu, L. Gu, Z. Liu and Y. Zhang, Metallic Vanadium Disulfide Nanosheets as a Platform Material for Multifunctional Electrode Applications, *Nano Lett.*, 2017, **17**, 4908–4916.

44 Y. Ma, Y. Dai, M. Guo, C. Niu, Y. Zhu and B. Huang, Evidence of the Existence of Magnetism in Pristine VX₂ Monolayers (X = S, Se) and Their Strain-Induced Tunable Magnetic Properties, *ACS Nano*, 2012, **6**, 1695–1701.

45 Y. Li, L. Su, Y. Lu, Q. Luo, P. Liang, H. Shu and X. Chen, High-throughput screening of phase-engineered atomically thin transition-metal dichalcogenides for van der Waals contacts at the Schottky–Mott limit, *InfoMat*, 2023, **5**, e12407.

46 B. Song, S. J. Yun, J. Jiang, J. Avila, K. Beach, W. Choi, Y.-M. Kim, D. Yoon, H. Terrones, Y. J. Song, M. C. Asensio, D. L. Duong and Y. H. Lee, Evidence of itinerant holes for long-range magnetic order in the tungsten diselenide semiconductor with vanadium dopants, *Phys. Rev. B*, 2021, **103**, 094432.

47 B. Stampfer, F. Zhang, Y. Y. Illarionov, T. Knobloch, P. Wu, M. Waltl, A. Grill, J. Appenzeller and T. Grasser, Characterization of Single Defects in Ultrascaled MoS₂ Field-Effect Transistors, *ACS Nano*, 2018, **12**, 5368–5375.

48 H. Ravichandran, T. Knobloch, A. Pannone, A. Karl, B. Stampfer, D. Waldhoer, Y. Zheng, N. U. Sakib, M. U. Karim Sadaf, R. Pendurthi, R. Torsi, J. A. Robinson, T. Grasser and S. Das, Observation of Rich Defect Dynamics in Monolayer MoS₂, *ACS Nano*, 2023, **17**, 14449–14460.

49 H. González-Herrero, J. M. Gómez-Rodríguez, P. Mallet, M. Moaied, J. J. Palacios, C. Salgado, M. M. Ugeda, J.-Y. Veuillen, F. Yndurain and I. Brihuega, Atomic-scale control of graphene magnetism by using hydrogen atoms, *Science*, 2016, **352**, 437–441.

50 B. Kiraly, E. J. Knol, W. M. J. van Weerdenburg, H. J. Kappen and A. A. Khajetoorians, An atomic Boltzmann machine capable of self-adaption, *Nat. Nanotechnol.*, 2021, **16**, 414–420.

51 T. Chen, J. van Gelder, B. van de Ven, S. V. Amitonov, B. de Wilde, H.-C. Ruiz Euler, H. Broersma, P. A. Bobbert, F. A. Zwanenburg and W. G. van der Wiel, Classification with a disordered dopant-atom network in silicon, *Nature*, 2020, **577**, 341–345.